Accepted Manuscript

Journal of Innovative Optical Health Sciences

Article Title:	Gates joint locally connected network for accurate and robust reconstruction in optical molecular tomography
Author(s):	Minghua Zhao, Yahui Xiao, Jiaqi Zhang, Xin Cao, Lin Wang
DOI:	10.1142/S179354582350027X
Received:	11 August 2023
Accepted:	27 September 2023
To be cited as:	Minghua Zhao *et al.*, Gates joint locally connected network for accurate and robust reconstruction in optical molecular tomography, *Journal of Innovative Optical Health Sciences*, doi: 10.1142/S179354582350027X
Link to final version:	https://doi.org/10.1142/S179354582350027X

Gates joint locally connected network for accurate and robust reconstruction in optical molecular tomography

Minghua Zhao,[1] Yahui Xiao,[1] Jiaqi Zhang,[1] Xin Cao,[2] and Lin Wang[1,*]

[1] *School of Computer Science and Engineering, Xi'an University of Technology, Xi'an, China*

[2] *School of Information Science and Technology, Northwest University, Xi'an 710127, China*

* *wanglin004@xaut.edu.cn*

Abstract: Optical molecular tomography (OMT) is a potential pre-clinical molecular imaging technique with applications in a variety of biomedical areas, which can provide non-invasive quantitative three-dimensional information regarding the tumor distribution in living animals. The construction of optical transmission models and the application of reconstruction algorithms in traditional model-based reconstruction processes have affected the reconstruction results, resulting in problems such as low accuracy, poor robustness, and longtime consumption. Here, a gates joint locally connected network method is proposed by establishing the mapping relationship between the inside source distribution and the photon density on surface directly, thus avoiding the extra time consumption caused by iteration and the reconstruction errors caused by model inaccuracy. Moreover, gates module was composed of the concatenation and multiplication operators of three different gates. It was embedded into the network aiming at remembering input surface photon density over a period and allowing the network to capture neurons connected to the true source selectively by controlling three different gates. To evaluate the performance of the proposed method, numerical simulations were conducted, whose results demonstrated good performance in terms of reconstruction positioning accuracy and robustness.

Keywords: Optical molecular tomography; gates module; positioning accuracy; robustness.

1. Introduction

Optical molecular imaging (OMI) is an imaging technology that collects the distribution and intensity of light flux on the surface of living organisms, which comes from optical molecular probes within the organisms.[1] OMI has been widely used in pre-clinical research due to its simplicity, high sensitivity, and non-invasive implementation.[2-4] However, it exits an obvious bottleneck that OMI cannot quantify the three-dimensional (3D) distribution of the optical signals in imaging objects. Thus, to overcome these limitations, optical molecular tomography (OMT) was further developed. OMT has completed a transformation from two-dimensional qualitative analysis to 3D quantitative analysis. By fusing structural information of organisms, quantitative distribution of optical probes within the organism can be provided.[5-7] Due to the sparsity of light distribution and the high heterogeneity of biological tissues, imaging accuracy has always been a challenge.[8-10]

To address the issues existing in 3D imaging methods, model-based methods mainly improve from two aspects. On the one hand, by improving the accuracy and efficiency of the optical transmission model, the problem of biological tissue heterogeneity can be solved, which improve the reconstruction results. For example, models such as diffusion approximation, simplified spherical harmonic approximation, and hybrid model are used for OMT.[11-14] On the other hand, strategies such as adding regularization constraints, allowing source regions and multispectral measurements are used for reconstruction, to overcome the ill posed problem caused by insufficient measurement data and high dimensionality of the model through iterative algorithms and increasing data volume.[15,16] Although these strategies have improved reconstruction performance and achieved accurate and efficient 3D reconstruction. However, there are still some errors in the approximate optical transmission model compared to the actual optical transmission process, which will be introduced into the final reconstruction results. Model based methods depend on iterative calculations to solve inverse problems, which is time-consuming. In addition, the accuracy and density of discretized mesh also affect the reconstruction accuracy and resolution seriously.

In recent years, the development of deep learning provides a new approach for optical 3D reconstruction. Due to its ability to abandon the construction of imaging models and system equations based on mathematical equations, it greatly reduces the pathological nature of 3D reconstruction mathematically and has been successfully applied in the field of OMT.[17-20] Zhang et al. proposed a method for CLT reconstruction using multi-layer fully connected neural networks (MFCNN),[21] and experiments showed that this method has better accuracy and stability compared to incomplete variables truncated conjugate gradient method. Guo et al. proposed an end-to-end 3D depth encoder decoder network,[22] which greatly improves image quality and significantly reduces reconstruction time. Li et al. proposed a deep convolutional framework based on the ResNet architecture for in vivo fluorescence reconstruction,[23] achieving high-quality image reconstruction with fewer parameters and relatively high speed. Meng et al. developed a K-nearest neighbor based locally connected (KNN-LC) network to reconstruct the distribution of fluorescence targets in fluorescence molecular tomography,[24] which achieved accurate reconstruction in a short period of time. Moreover, 15% gaussian noise was added to the KNN-LC network and achieved accurate source localization with noise interference. Cao et al. proposed an excitation-based fully connected network (EFCN) for the second near-infrared fluorescence molecular tomography with the excitation module and center of barycenter error are added to the network and the loss function to improve the positioning accuracy of the light source.[25] Furthermore, 10% Gaussian noise was added to test the robustness of EFCN. The results demonstrated that EFCN improved the quality of FMT reconstruction. However, these reconstruction methods based on deep learning generally lack robustness verification, and their noise resistance needs to be further strengthened. Therefore, 3D imaging methods still need to be further strengthened in terms of network efficiency, reconstruction accuracy, and robustness.

In this paper, inspired by long short-term memory network,[26] which used to deal with a series of sequence data and allows the network to remember inputs over a period of time, a gates joint locally connected network (GLCN) was proposed. GLCN is composed of a locally connected (LC) network with gate modules embedded aiming to achieve higher accuracy and robustness of OMT reconstruction. The gates module can control different weights for each neuron,

enabling the network to selectively capture neurons connected to the true source. To evaluate the performance of GLCN, numerical simulation experiments were conducted. The IVTCG and MFCNN methods were adopted as the baseline for comparisons. The reconstruction results showed that GLCN outperformed in terms of localization accuracy and robustness.

2. Methods

2.1. *Glcn network architecture*

Inspired by long short-term memory network, we tried to use a similar backbone to achieve OMT reconstruction. The whole GLCN architecture is composed of a gate layer with three gate units, a hidden layer and three LC layers (Fig. 1(a)). The number of neurons in the hidden layer and three LC layers is 256, 128, 64, and 3, respectively. The gates module can control and capture the input and output of network information flow by three different gate units (Fig. 1(b)). Compared with standard fully connected network, locally connected layer has the advantage of reducing the quantity of parameter computation. The different network layers of GLCN are partially connected by the dashed line to achieve the neuron information transfer, and this dimensionality reduction operation facilitates GLCN to obtain more accurate results. The surface photon energy Φ was obtained by CCD and fed into the network as the input, and the output is the distribution of reconstruction source X . The whole GLCN-based OMT reconstruction framework as follows:

$$X = f(\Phi), \tag{1}$$

Where f represents GLCN model, which represents the nonlinear relationship between the surface energy distribution and the light source. Φ represents the surface measurements with a dimension of $n \times 1$, and n is the number of nodes in a discrete organism. Further, the inverse problem can be defined as follows:

$$\min \left\| f_\theta(\mathrm{y} \mid \theta) \right\|_2^2, \tag{2}$$

where f_θ is the result of the reconstruction network with parameters vector θ. y represents the ground-truth distribution information. The weight θ is iteratively updated by minimizing the loss between y and f.

The structure of gates module can be calculated as follows:

$$Gate1_{out} = \sigma(W(Gate_{in})), \tag{3}$$

$$Gate2_{out} = Gate1_{out} + \delta(\sigma(W(Gate_{in}))), \tag{4}$$

$$Gate3_{out} = \sigma(W(Gate_{in})), \tag{5}$$

$$Gate_{out} = Gate3_{out}(\delta(Gate2_{out})), \tag{6}$$

where $Gate_{in}$ and $Gate_{out}$ denote the input and output of gate layer, respectively; $Gate1_{out}$, $Gate2_{out}$ and $Gate3_{out}$ represent the output of the first, second, and third gate units, respectively; W refers to network weights; σ, δ are sigmoid, and tanh activation, respectively.

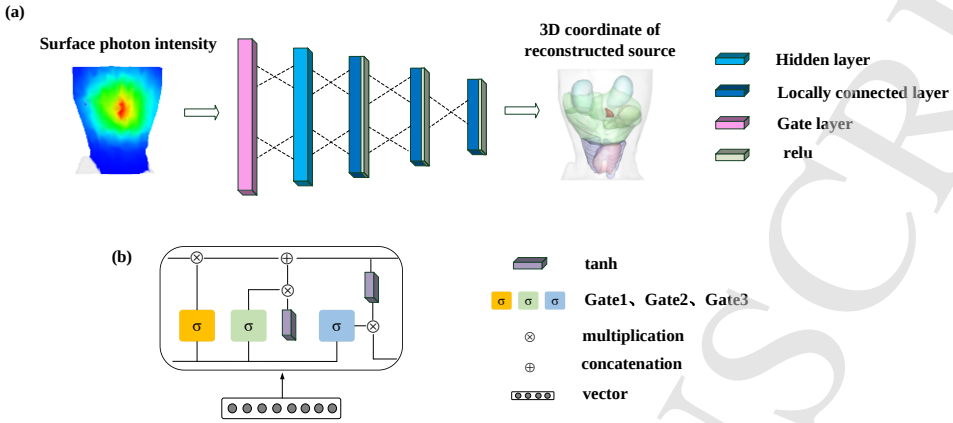

Fig. 1. Schematic illustration of GLCN architecture. (a) the general flow chart of GLCN for OMT reconstruction. (b) structure of gates module.

2.2. *Dataset collection*

Considered that deep learning networks are data-driven methods, accumulating ample training samples is necessary. However, directly acquiring the actual distribution of source and the surface photon measurements in vivo experiments is unpractical. In this study, we adopted the Monte Carlo (MC) method to generate the simulation samples.[27,28] MC method can provide both surface photon measurements and standard of actual distribution of source. In addition, all data sets used in this paper
are collected using standard grids discretization from the numerical cylinder model (4626 nodes and 25840 tetrahedrons) and the numerical mouse model (13092 nodes and 67612 tetrahedrons).
In the numerical experiments, this paper generates samples by randomly setting spherical source targets with the radius of 1mm. For numerical cylinder experiments, 1190 single source samples were produced by the Molecular Optical Simulation Environment (MOSE v2.3)[28] with 190 samples for test set randomly. Meanwhile, 960 single source samples were produced for numerical mouse experiments, in which 96 random samples were used as the test set.
As for the dual-source simulation experiments, data augmentation method was adopted. The dual sources samples were produced by randomly choosing and adding two corresponding single source samples. The data augmentation method can be calculated as follows:

$$\Phi_{d_s} = \sum_{i \in S} \Phi_i, \tag{7}$$

$$X_{d_s} = \sum_{i \in S} X_i, \tag{8}$$

Where Φ_{d_s}, X_{d_s} represent the surface photon energy and the inside source of dual sources assembled, respectively. Φ_i means the surface photon of the i_{th} single source. X_i refers the i_{th} single source. S is the set of selected single-source samples.
Finally, 8820 dual-source samples were collected for the numerical cylinder experiments. During the experiment, 1470 samples were selected randomly for the test set, while the rest of 7350 samples were collected as training set to generate

GLCN. Similarly, 8144 dual-source samples were produced for the numerical mouse experiments with 880 dual-source samples were chosen for test set.

2.3. *Network implementation details and evaluation index*

All experiments in this article were accomplished on a computer equipped with an RTX 3080 Ti GPU and a 3.2 GHz Intel Core i9 CPU. The training and testing of deep learning networks are implemented by Pytorch and Python 3.7. The mean square error (MSE)[29] was adopted as the loss function considering that spatial location is of great significance for OMT reconstruction and directly affects the pre-clinical application.

$$L_{mse} = \frac{1}{n}\sum(\hat{y}_i - y_i)^2, \tag{9}$$

where $\hat{y}_i$ and y_i represent the network's prediction and the ground-truth label of i_{th} dataset sample, respectively; n represents the set of elements of i_{th} dataset sample. Besides, Adam algorithm[30] (learning rate = 0.001, β_1:0.9, β_2:0.99) was adopted as the optimization function of GLCN.

The PE evaluation index was used in the experiments to measure the reconstruction performance. PE means the position error, which is calculated as the Euclidean distance between the reconstructed source and the ground-truth:

$$PE = \left\| ED(X_r) - ED(X_t) \right\|, \tag{10}$$

Where X_r and X_t means the coordinates of the reconstructed and true sources, respectively. The smaller PE means the more accurate reconstruction result.

3. Results

In this section, numerical emulation experiments were used for evaluate the performance of GLCN. IVTCG and MFCNN were used as comparisons. Firstly, numerical simulation experiments were conducted on single and dual light source cylinders. In additional, the results of GLCN in digital mouse simulations were presented, the experiments were also divided into single and dual source experiments. Finally, we listed the reconstruction time of these methods in single source simulation experiments to compare the reconstruction efficiency.

3.1. *Single-source reconstruction on numerical cylinder simulation*

For a representative sample with its axis length along z axes was 12 mm, where the light source is located. Fig. 2(a) shows the 3D view and 2D section images (slice at z = 12 mm) of the reconstructed source using three methods. From the reconstructed result, the IVTCG reconstructed result is over-sparse and GLCN is smoother relatively. The result of MFCNN has with significant overlap with the distribution of real light source.

To evaluate the anti-noise ability of the proposed method, different levels (30%, 60%, 90%) of gaussian noise were added to the measurement data in simulation experiments with test single samples. As displayed in Fig. 2(b-d), the results of three methods all show changes with noise interference. IVTCG appears blur and divergence. While MFCNN and GLCN gain distinct results. Compared with MFCNN, GLCN is closer to the true source.

Besides, the quantitative results (mean and standard deviation (SD)) of three methods are demonstrated in Fig. 3. As shown, GLCN achieves better reconstruction performance with a PE down to 0.36±0.18 mm. With the noise level ranging from 0%-30%, the PE of IVTCG, MFCNN and GLCN increase by 21.1%, 11.1%, 5.6%, respectively. When the noise level is added to 60% and 90%, the PE of the three methods shows significant changes. However, GLCN still has the minimum PE, which are 0.51±0.19 and 0.78±0.28, respectively. The results indicate that GLCN possesses superior performance in terms of localization accuracy and anti-noise interference.

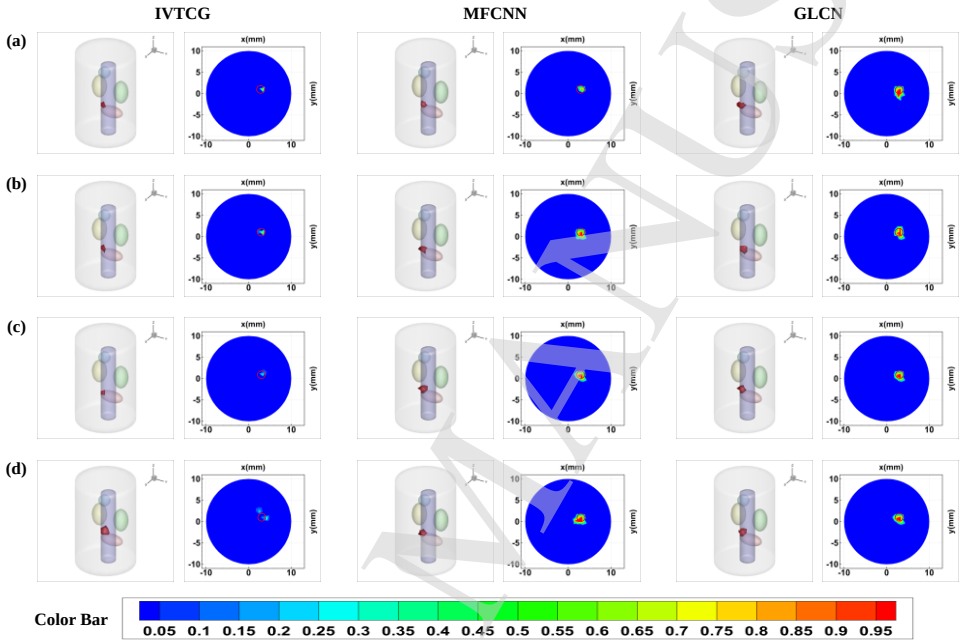

Fig. 2. OMT reconstruction results of single sources with different level of noise interference using different methods. (a) displays the 3D view and transverse sections of the reconstructed sources given by IVTCG, MFCNN and GLCN, respectively. (b-d) depict the 3D view and transverse sections of reconstructed sources with 30%, 60%, 90% gaussian noise given by IVTCG, MFCNN and GLCN, respectively. The red cycle represents the true source region.

3.2. *Dual-source reconstruction on numerical cylinder simulation*

The localization accuracy of GLCN is further examined by reconstructing dual-source samples on numerical cylinder simulations. Three dual-source samples with different edge-to-edge distances (EEDs) were reconstructed for display. Their axis length along z axes is 18, 20, 20 mm, respectively. Fig. 4 display the 2D transverse sections (taken from z = 18, 20, 20 mm separately) and the 3D reconstruction effects using three different methods. It can be seen from the Fig. 4 that when the EED is 3mm, the result of IVTCG showed artifact. At this point, MFCNN and GLCN can obtain the clearer reconstruction results. When the EED is 2 mm, IVTCG could not correctly reconstruct the light sources. In this case, although both MFCNN and GLCN could distinguish the light sources, one of the reconstruction sources of MFCNN is not significant. When the EED is as small as 1mm, IVTCG cannot recognize these two light sources, and compared to MFCNN, GLCN is closer to the real source region.

Furthermore, the quantitative error comparison (Fig. 5) shows that the average PE of GLCN compared to EFCN and IVTCG are 33.3% -57.8% and 10.7% -21.8%, respectively. As the EEDs decrease, the average PE of all three methods increase by varying degrees. As shown in the Fig. 5, the error of IVTCG is the highest. However, GLCN gets the lowest average PE of 0.12 mm, 0.16 mm and 0.26 mm, which indicates that the GLCN provides higher accuracy to reconstruct dual-source. Moreover, the PE value of reconstructed sources S1 and S2 by IVTCG has obvious difference. While the PE value of reconstructed sources S1 and S2 by MFCNN and GLCN approaches much relatively. These results all proved the superiority of GLCN in the reconstruction of dual-source.

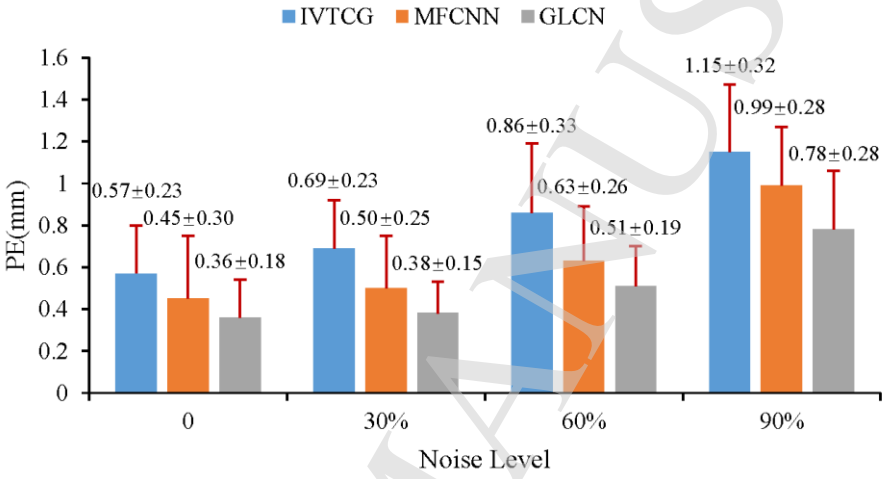

Fig. 3. Quantitative results including the mean and standard deviation (SD) of single-source reconstruction with 0, 30%, 60%, 90% gaussian noise given by IVTCG, MFCNN and GLCN, respectively.

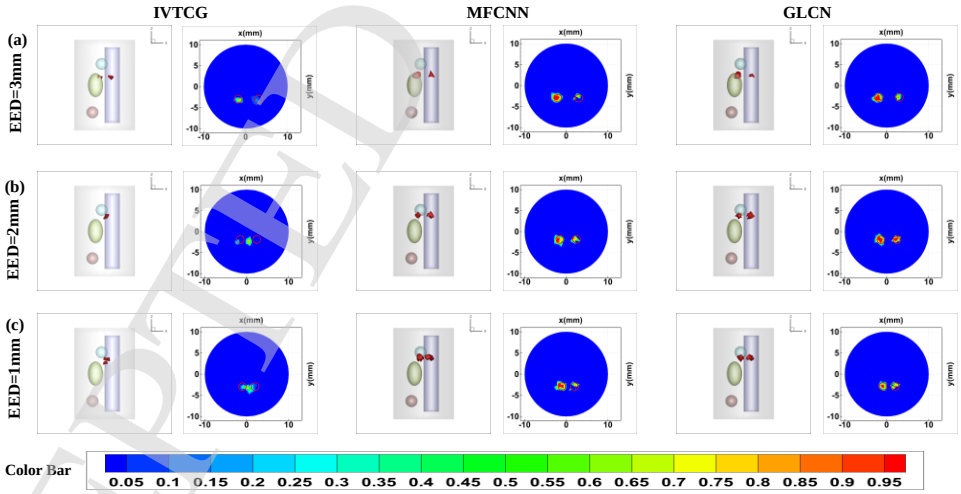

Fig. 4. OMT reconstruction results of dual-source with different Edge-to-Edge Distances (EEDs). (a-c) demonstrate the reconstructed dual-source using different methods when EEDs are 3, 2 and 1mm, respectively. Both 3D rendering and 2D transverse sections are depicted for comparisons. The red cycle represents the true source region.

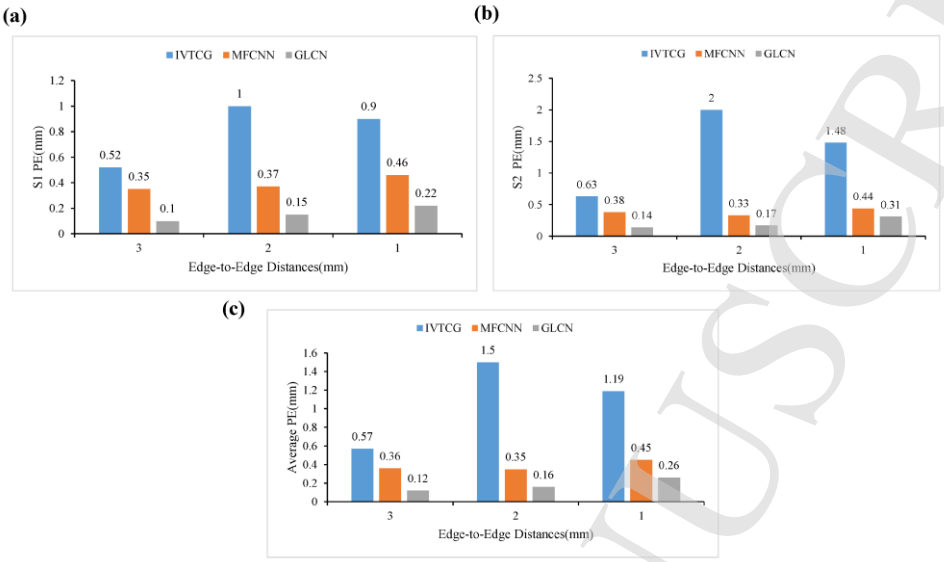

Fig. 5. Quantitative analysis was conducted on dual-source reconstruction utilizing EEDs ranging from 3 to 1 mm. (a) and (b) present the PE of reconstructed sources S1 and S2, respectively. (c) shows the average PE of S1 and S2.

3.3. *Single-source reconstruction on digital mouse simulation*

For a representative sample with a z-axis of 13.5 mm, Fig. 6(a) shows the 3D view and 2D section images (slice at z=13.5 mm) of reconstructed source by three methods. The result of MFCNN is closer to the true source and the second is GLCN, then IVTCG.

Furthermore, 30%, 60% and 90% Gaussian noise were added to the surface photon density of the single-source sample to test the robustness of GLCN (Fig. 6(b-d)). Under 30% Gaussian noise, the reconstructed results of three methods remained the same as those without noise in display. With the 60% Gaussian noise, the result of IVTCG appeared artifact. MFCNN and GLCN still could correctly reconstruct the sources. When Gaussian noise is added to 90% level, the experimental results show that only GLCN successfully reconstructs the light source, while the other two methods have poor reconstruction results. These results demonstrate that GLCN has significant advantages in resisting noise interference.

In order to quantitatively compare the performance of reconstruction results, Fig. 7 displays the mean and standard deviation (SD) of PE. GLCN obtains the PE of 0.38±0.13 mm that proves the superiority of GLCN on reconstruction accuracy for OMT. With the Gaussian noise added to 30% level, the PE of the test sample reconstructed by three methods has not much change compared to that without noise. From 60% level Gaussian noise on, the PE of three methods has significant increase. However, GLCN still gains the whole minimum PE (0.37±0.15 mm, 0.55±0.20 mm, 0.79±0.23 mm), indicating the excellent anti-noise ability of the network.

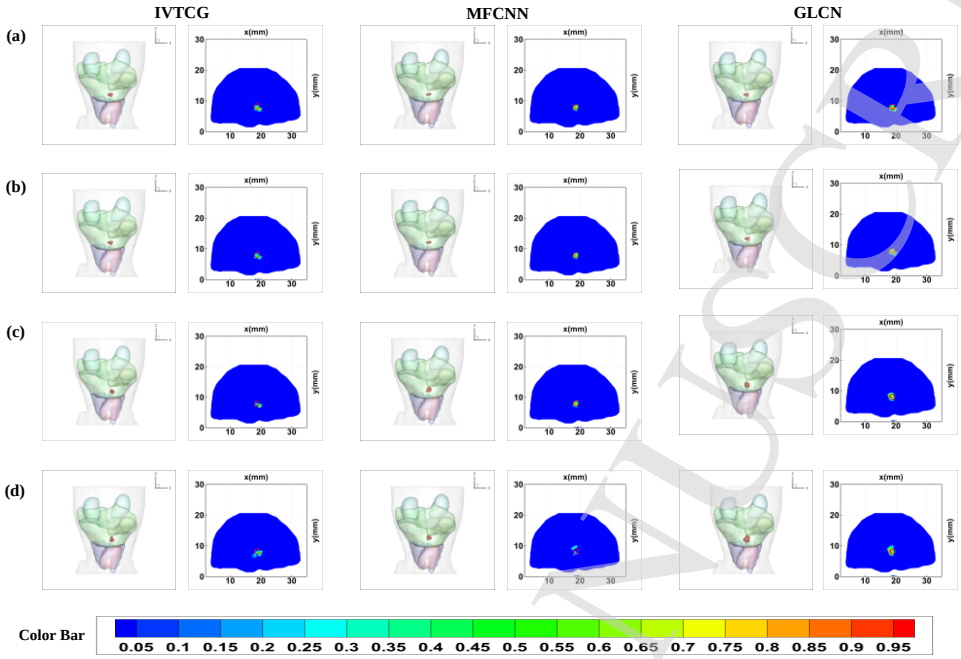

Fig. 6. OMT reconstruction results of single sources with varying noise interference levels using different methods. (a) displays the 3D view and transverse sections of the reconstructed sources given by IVTCG, MFCNN and GLCN, respectively. (b-d) demonstrate the 3D view and transverse sections of reconstructed sources with 30%, 60%, and 90% gaussian noise using IVTCG, MFCNN and GLCN, respectively. The red cycle represents the true source regions.

3.4. *Dual-source reconstruction on digital mouse simulation*

Dual-source with different edge-to-edge distances (EEDs) samples were implemented to test the reconstruction ability of GLCN. Fig. 8 shows the 3D view and 2D section images (slice at z=12.5 mm) of reconstructed source by three methods. When the EED is 3 mm, the reconstruction results of IVTCG show that the two light sources are not significant. Although the results of MFCNN and GLCN exits problems such as over-spare and over-smooth, they can clearly distinguish between the two light sources. And obviously, GLCN is closer to the true source region. When the EED is 2 mm, all three methods can clearly distinguish between dual light sources. GLCN has better general overlap than the other two methods. When the EED decreases to 1mm, adhesion occurs in the IVTCG reconstruction results. There is a significant deviation in the reconstruction position of the MFCNN dual light source. In contrast, GLCN reconstruction results are closer to the true light source area.

Quantitative comparisons demonstrated the superior performance of GLCN over the other method in localization accuracy (Fig. 9). The average PE of GLCN compared to MFCNN and IVTCG are 23.3%-59.2% and 10.9%-69.9%, respectively. In addition, when the edge-to-edge distance of dual-source equals to 1 mm, the average PE of GLCN wonderfully reached to 0.1 mm. These results revealed that GLCN had a better ability for dual-source reconstruction.

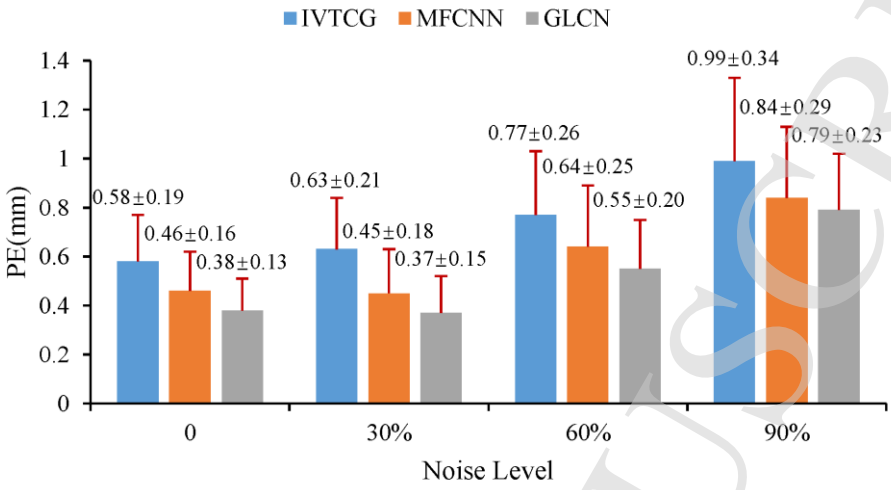

Fig. 7. Quantitative results including the mean and standard deviation (SD) of single-source reconstruction with 0, 30%, 60%, 90% gaussian noise given by IVTCG, MFCNN and GLCN, respectively.

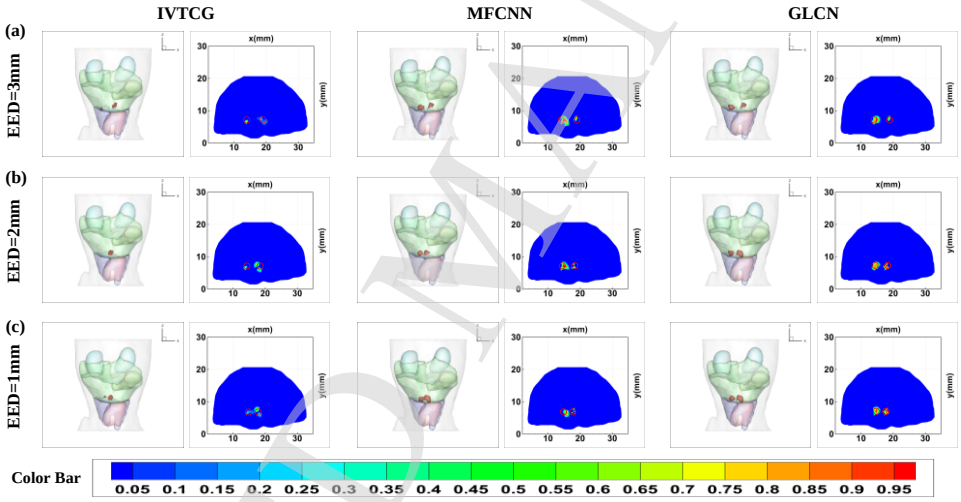

Fig. 8. OMT reconstruction results of dual-source with different Edge-to-Edge Distances (EEDs). (a-c) depict the reconstructed sources using various methods at EEDs of 3, 2 and 1mm, respectively. Both 3D rendering and 2D transverse sections were presented for comparisons. The red cycle represents the true source region.

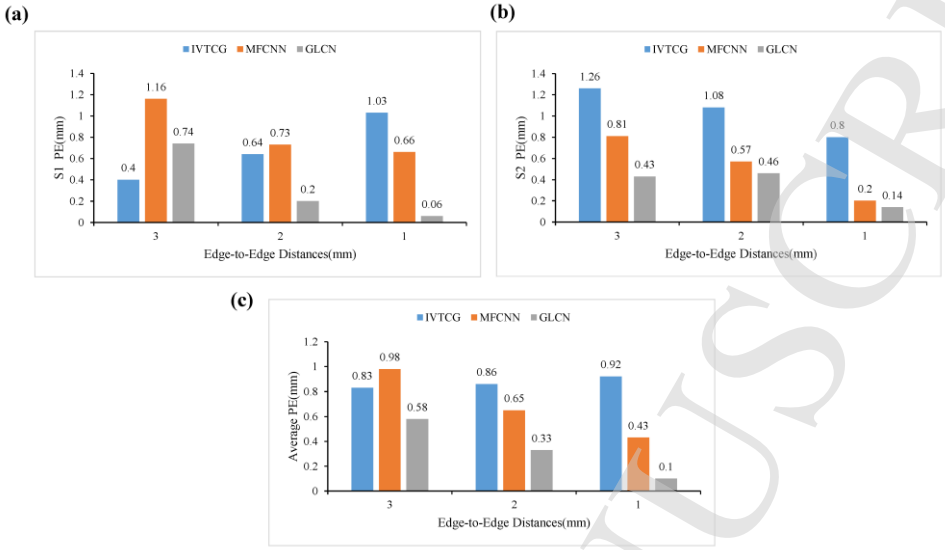

Fig. 9. Quantitative analysis was conducted on dual-source reconstruction utilizing EEDs ranging from 3 to 1 mm. (a) and (b) display the PE of reconstructed sources S1 and S2, respectively. (c) shows the average PE of S1 and S2.

3.5. *Reconstruction time*

The reconstruction time of three single-source methods for numerical cylinder and mouse simulations was calculated to access the efficiency of GLCN's reconstruction (Table 1). Both model-based and data-driven methods required considerable preparation time. IVTCG method needed to model the precise forward model and solve and optimize the inverse problem through lots of iteration steps. MFCNN and GLCN methods needed to prepare and perform the training samples and the training process. Only the test time of MFCNN and GLCN methods and the iterative calculation time of IVTCG were collected for comparisons in this study. As shown in Table 1, the mean and standard deviation (SD) of reconstruction time of IVTCG (4.79±0.20 s) was nearly 6~7 times that of MFCNN (0.66±0.03 s) and GLCN (0.76±0.04 s) on cylinder simulation experiments. And on mouse simulation experiments, the reconstruction time (mean and standard deviation (SD)) accorded by IVTCG (19.59±0.41 s) was nearly 25~30 times that of MFCNN (0.64±0.03 s) and GLCN (0.78±0.04 s). These results demonstrated that data-driven methods had much advantage on reconstruction efficiency than the model-based methods.

Table 1. Time Cost Analysis for Single Source Reconstruction (in units of second).

Methods	IVTCG	MFCNN	GLCN
cylinder	4.79±0.20	0.66±0.03	0.76±0.04
mouse	19.59±0.41	0.64±0.03	0.78±0.04

4. Discussion

Optical molecular tomography (OMT) has been utilized to reconstruct the 3D distribution of targets within living animals. However, the ill-posedness of the inverse problem usually leads to inaccurate and low-robust reconstructions. Consequently, in this study, we proposed a deep learning approach (GLCN) to

solve the inverse problem of optical molecular tomography. Different from the conventional methods that need to model the inverse construction process. GLCN avoids additional calculation errors and improves reconstruction efficiency. In addition, GLCN brings into gates module to implement the reconstruction process. Compared to MFCNN, this module will benefit the network to capture the crucial information of neurons that relates to the true region selectively.

Two kinds of numerical simulation experiments were carried out to evaluate the performance of GLCN from both qualitative and quantitative aspects. For single source reconstruction, GLCN obtains best reconstruction performance with a PE down to 0.36±0.18 mm and 0.38±0.13 mm for cylinder and digital mouse-based simulation experiments, respectively. In contrast, IVTCG gains the average PE of 0.57±0.23 mm and 0.58±0.19 mm. MFCNN gains the average PE of 0.45±0.30 mm and 0.46±0.16 mm. These results proved GLCN is superior to the other two methods on accuracy and robustness (having small error fluctuation). For dual-source reconstruction, GLCN gets the lowest average PE of 0.12 mm, 0.16 mm, and 0.26 mm for EED equaling to 3mm, 2mm, 1mm respectively in cylinder-based simulation experiments. In digital mouse simulation experiments, when the EED of dual-source equals to 1 mm, the average PE of GLCN wonderfully reached to 0.1 mm. These results showed that the proposed GLCN method also outperforms the other two methods in the dual-source reconstruction.

In addition, 30%, 60% and 90% noise interference were added on the surface photon density to access the anti-noise ability of GLCN in the single-source numerical simulation experiments. Conventional method (IVTCG) appeared obvious change when gaussian noise reaches to 30% level, while MFCNN and GLCN appeared obvious change until noise level reaches to 60%. Moreover, compared to MFCNN, GLCN robustly reconstructs the single source that is more accurate and higher overlap with overall lower PE. These results further prove the superior robustness of the GLCN.

Nevertheless, there are also some challenges. Firstly, the number of nodes used in cylinder and digital mouse models were 4, 626 and 13, 092, respectively. The number of grids will affect the reconstruction results. We believe that finer mesh will facilitate to improve the accuracy of the reconstruction and will not affect the speed of reconstruction for deep learning methods. Secondly, GLCN, as a method of deep learning, which needs a pre-trained standard mesh model for reconstruction. Once the target changes, the reconstruction performance of GLCN will be greatly reduced. Thus, it is necessary for us to improve the generalization of network. Lastly, GLCN exits some defects on the reconstruction morphology. In the future, we will continue to work towards these challenging directions.

5. Conclusion

In summary, we proposed a gates joint locally connected network (GLCN) to implement the accurate and robust reconstruction of OMT. The ill-posedness of OMT could be greatly reduced with the introduction of gates module. Meanwhile, gates module could improve the reconstruction accuracy and robustness of OMT. Two different kinds of numerical simulation experiments confirmed that GLCN can obtain the more accurate and robust reconstruction results compared with the other two methods. This study will be a trivial exploration of OMT reconstruction. In the future, we will promote the proposed method applying to real mice-based applications.

Acknowledgments

This study was supported by National Natural Science Foundation of China (62101439) and Key Research and Development Program of Shaanxi (2023-YBSF-289).

Conflicts of Interest

The authors declare that there are no conflicts of interest relevant to this article.

References

1. R. John, R. Rezaeipoor, S. G. Adie, E. J. Chaney, A. L. Oldenburg, M. Marjanovic, J. P. Haldar, B. P. Sutton, S. A. Boppart, "In vivo magnetomotive optical molecular imaging using targeted magnetic nanoprobes," *Proceedings of the National Academy of Sciences* **107**(18), 8085–8090 (2010).
2. C. Chi, Y. Du, J. Ye, D. Kou, J. Qiu, J. Wang, J. Tian, X. Chen, "Intraoperative imaging-guided cancer surgery: from current fluorescence molecular imaging methods to future multi-modality imaging technology," *Theranostics* **4**(11), p. 1072 (2014).
3. G. S. Mitchell, P. T. Lloyd, S. R. Cherry, "Cerenkov luminescence and pet imaging of 90y: capabilities and limitations in small animal applications," *Physics in Medicine & Biology* **65**(6), p. 065006 (2020).
4. D. Fan, X. Zhang, L. Zhong, X. Liu, Y. Sun, H. Zhao, B. Jia, Z. Liu, Z. Zhu, J. Shi et al., "68ga-labeled 3prgd2 for dual pet and cerenkov luminescence imaging of orthotopic human glioblastoma," *Bioconjugate chemistry* **26**(6), 1054–1060 (2015).
5. Y. Gao, K. Wang, S. Jiang, Y. Liu, T. Ai, J. Tian, "Bioluminescence tomography based on gaussian weighted laplace prior regularization for in vivo morphological imaging of glioma," *IEEE transactions on medical imaging* **36**(11), 2343–2354 (2017).
6. H. Liu, X. Yang, T. Song, C. Bao, L. Shi, Z. Hu, K. Wang, J. Tian, "Multispectral hybrid cerenkov luminescence tomography based on the finite element spn method," *Journal of biomedical optics* **20**(8), p. 086007 (2015).
7. H. Guo, Y. Hou, X. He, J. Yu, J. Cheng, X. Pu, "Adaptive hp finite element method for fluorescence molecular tomography with simplified spherical harmonics approximation," *Journal of Innovative Optical Health Sciences* **7**(02), p. 1350057 (2014).
8. E. Ciarrocchi, N. Belcari, "Cerenkov luminescence imaging: physics principles and potential applications in biomedical sciences," *EJNMMI physics* **4**(1), 1–31 (2017).
9. B. Zhang, W. Yin, H. Liu, X. Cao, H. Wang, "Bioluminescence tomography with structural information estimated via statistical mouse atlas registration," *Biomedical Optics Express* **9**(8), 3544–3558 (2018).
10. J. Yu, B. Zhang, I. I. Iordachita, J. Reyes, Z. Lu, M. V. Brock, M. S. Patterson, J. W. Wong, K. K.-H. Wang, "Systematic study of target localization for bioluminescence tomography guided radiation therapy," *Medical physics* **43**(5), 2619–2629 (2016).
11. W. Cong, G. Wang, D. Kumar, Y. Liu, M. Jiang, L. V. Wang, E. A. Hoffman, G. McLennan, P. B. McCray, J. Zabner et al., "Practical reconstruction method for bioluminescence tomography," *Optics Express* **13**(18), 6756–6771 (2005).
12. Y. Lu, A. Douraghy, H. B. Machado, D. Stout, J. Tian, H. Herschman, A. F. Chatziioannou, "Spectrally resolved bioluminescence tomography with the third-order simplified spherical harmonics approximation," *Physics in Medicine & Biology* **54**(21), p. 6477 (2009).
13. D. Yang, X. Chen, S. Ren, X. Qu, J. Tian, J. Liang, "Influence investigation of a void region on modeling light propagation in a heterogeneous medium," *Applied optics* **52**(3), 400–408 (2013).

14. L. Wang, X. Cao, Q. Ren, X. Chen, X. He, "Hybrid model based unified scheme for endoscopic cerenkov and radio-luminescence tomography: Simulation demonstration," *Journal of Applied Physics* **123**(18), p. 184701 (2018).
15. H. Yi, D. Chen, W. Li, S. Zhu, X. Wang, J. Liang, J. Tian, "Reconstruction algorithms based on l 1-norm and l 2-norm for two imaging models of fluorescence molecular tomography: a comparative study," *Journal of Biomedical Optics* **18**(5), 056013–056013 (2013).
16. H. Guo, X. He, M. Liu, Z. Zhang, Z. Hu, J. Tian, "Weight multispectral reconstruction strategy for enhanced reconstruction accuracy and stability with cerenkov luminescence tomography," *IEEE transactions on medical imaging* **36**(6), 1337–1346 (2017).
17. Y. Gao, K. Wang, Y. An, S. Jiang, H. Meng, J. Tian, "Nonmodel-based bioluminescence tomography using a machine-learning reconstruction strategy," *Optica* **5**(11), 1451–1454 (2018).
18. S. P. Davis, S. Kumar, Y. Alexandrov, A. Bhargava, G. da Silva Xavier, G. A. Rutter, P. Frankel, E. Sahai, S. Flaxman, P. M. French et al., "Convolutional neural networks for reconstruction of undersampled optical projection tomography data applied to in vivo imaging of zebrafish," *Journal of Biophotonics* **12**(12), p. e201900128 (2019).
19. F. Yang, T.-a. Pham, H. Gupta, M. Unser, J. Ma, "Deep-learning projector for optical diffraction tomography," *Optics express* **28**(3), 3905–3921 (2020).
20. J. Yoo, S. Sabir, D. Heo, K. H. Kim, A. Wahab, Y. Choi, S.-I. Lee, E. Y. Chae, H. H. Kim, Y. M. Bae et al., "Deep learning diffuse optical tomography," *IEEE transactions on medical imaging* **39**(4), 877–887 (2019).
21. Z. Zhang, M. Cai, Y. Gao, X. Shi, X. Zhang, Z. Hu, J. Tian, "A novel cerenkov luminescence tomography approach using multilayer fully connected neural network," *Physics in Medicine & Biology* **64**(24), p. 245010 (2019).
22. L. Guo, F. Liu, C. Cai, J. Liu, G. Zhang, "3d deep encoder–decoder network for fluorescence molecular tomography," *Optics letters* **44**(8), 1892–1895 (2019).
23. D. Li, C. Chen, J. Li, Q. Yan, "Reconstruction of fluorescence molecular tomography based on graph convolution networks," *Journal of Optics* **22**(4), p. 045602 (2020).
24. H. Meng, Y. Gao, X. Yang, K. Wang, J. Tian, "K-nearest neighbor based locally connected network for fast morphological reconstruction in fluorescence molecular tomography," *IEEE transactions on medical imaging* **39**(10), 3019–3028 (2020).
25. C. Cao, A. Xiao, M. Cai, B. Shen, L. Guo, X. Shi, J. Tian, Z. Hu, "Excitation-based fully connected network for precise nir-ii fluorescence molecular tomography," *Biomedical Optics Express* **13**(12), 6284–6299 (2022).
26. A. Graves, A. Graves, "Long short-term memory," *Supervised sequence labelling with recurrent neural networks*, 37–45 (2012).
27. S. Bartel, A. H. Hielscher, "Monte carlo simulations of the diffuse backscattering mueller matrix for highly scattering media," *Applied Optics* **39**(10), 1580–1588 (2000).
28. S. Ren, X. Chen, H. Wang, X. Qu, G. Wang, J. Liang, J. Tian, "Molecular optical simulation environment (mose): a platform for the simulation of light propagation in turbid media," *PloS one* **8**(4), p. e61304 (2013).
29. V. H. Vu, "On the infeasibility of training neural networks with small mean-squared error," *IEEE Transactions on Information Theory* **44**(7), 2892–2900 (1998).
30. D. P. Kingma, J. Ba, "Adam: A method for stochastic optimization," *arXiv preprint arXiv:1412.6980* (2014).